Eleventh International Conference on Computational Fluid Dynamics (ICCFD11), Maui, HI, USA 2022

ICCFD11-2022-2602

Study of Graphite Ablation at Arc-Jet Conditions using Finite-Rate and Equilibrium Chemistry Models

Aleksander L. Zibitsker* and Alexandre Martin*
* University of Kentucky, Lexington, Kentucky, 40506 USA

Joel A. McQuaid† and Christoph Brehm†
† University of Maryland, College Park, Maryland, 20742 USA.

Grant Palmer‡
‡ Analytical Mechanics Associates at NASA Ames Research Center, Moffett Field, CA 94035 USA

Benjamin Libben‖ and Eric Stern‖
‖ NASA Ames Research Center, Moffett Field, CA 94035 USA

Abstract: Moving at hypersonic speeds through the atmosphere generates immense amount of heat that triggers thermo-chemical non-equilibrium effects in the flow approaching the vehicle and leads to surface chemical reactions that cause ablation and consume the material mass. This complex behavior and interaction of the aerothermal environment with a graphite surface is computationally modeled in the present work using a fully-coupled simulation between flow solver CHAMPS NBS-Cart and material response solver KATS-MR. In this study, we account for the thermo-chemical non-equilibrium effects occurring in the flow and use an 11-species air-carbon reaction model to simulate the ablation of the material. The reactions at the surface such oxidation, nitridation and recombination are modeled with a newly developed air-carbon reaction model. The coupled simulation is applied to study two experimental cases performed at IHF arc-jet facility at NASA Ames research center. The obtained results are compared against the measured data of surface recession, as well as surface and in-depth temperatures. Additionally, uncoupled simulations, performed with equilibrium chemistry at the wall, point out the substantial differences between the coupled and uncoupled solutions, leading to higher deviation of the predicted temperatures. Overall, we show excellent agreement between the coupled simulation predictions and the experimental data in all measured quantities.

Keywords: Hypersonic flow, Ablation, Graphite, Numerical Algorithms.

1 Introduction

Moving through the atmosphere at hypersonic speeds generates an immense amount of heat as a result of air compression upstream of the vehicle. This leads to extremely high temperatures in the shock layer that triggers thermo-chemical non-equilibrium effects in the flow approaching the vehicle surface. In the case of carbon based thermal protection materials, the extreme heating and chemically reacting flow lead to oxidation and nitridation reactions between the dissociated air species and the material surface causing material consumption. At higher surface temperatures, phase change of the carbon material occurs and sublimation reactions lead to additional and increasingly higher material mass loss at the surface.

The engineering level analysis and design of thermal protection materials for atmospheric entry applications is typically performed with uncoupled analysis of the material thermal response. The analysis relies on

the use of engineering correlations to apply the heat flux boundary condition and equilibrium chemistry and equal mass and heat transfer coefficients for the ablation physics. This analysis also relies on the assumption that the change of the shape of the material doesn't significantly affect the shape of the applied boundary conditions.

Performing a coupled analysis of the fluid-ablation interaction is not a trivial problem and requires the resolution of different scales in the flow and material physics. The coupling scheme between the solvers is another source of research on how to accurately exchange the boundary conditions between the solvers and also preserve the computational cost of the simulation. Multiple researchers have developed and simulated coupled ablation problems with different levels of fidelity. One of the common coupling approaches, requiring minimal intrusiveness into the computational solvers. is to use the traditional equilibrium ablation physics on the material side and apply explicitly the heat flux and pressure boundary conditions from the coupled flow solution without exchanging the blowing species. Chen et al. [1] has explored a loosely coupled approach where the boundary conditions were exchanged only after a certain amount of surface recession has occurred. After each transfer of the new surface geometry the flow mesh was adjusted and a new converged solution was applied. Surface thermo-chemical interactions and blowing effects were incorporated in the material response code by using ablation tables, the surface energy balance with the heat transfer coefficient, and the blowing reduction parameter. This approach showed to be effective in predicting the effect of surface topology changes on the profile of the flow boundary conditions.

Higher fidelity coupled simulations include finite-rate chemistry incorporated at the material surface and the interaction of the blowing species with the flow environment. A less computationally expensive approach was performed by Chen and Milos [2] to study ablation of graphite in arc-jet flow. Instead of solving the material conduction problem on a moving mesh, the surface temperature is computed by assuming a steady state energy balance at the surface and a non-moving wall. The full surface state is obtained from solving the surface mass balance equation and finite-rate chemistry. This approach is versatile as it allows for the use of different surface kinetics models that are completely implemented on the flow solver side and no need for the material response solver is required. A similar approach was implemented in a prior work in Ref. 3. In this case though, the in-depth material temperatures are unknown and the prediction of the surface temperature from the steady state energy balance could introduce inaccuracies in the solution. In the mentioned study by Chen and Milos, modeling of graphite ablation has relied on the use of heritage surface kinetics models developed by Park in the late 70's [4] and the Zhluktov-Abe model [5] from the end of 90's. Using the aforementioned finite-rate models, ablation of a graphite sphere-cone sample was significantly under-predicted, implying that important surface kinetics mechanisms were not captured in the simulation.

In this work, we employ a recently developed coupled interaction simulation between CHAMPS NBS-Cart and KATS-MR solvers [3, 6] to simulate ablation of graphite at the arc-jet flow conditions. The finite-rate surface chemistry employs the recently developed air-carbon reaction model by Prata et al. [7]. This model was constructed based on the data from a continuous beam experiment of oxygen and nitrogen species impinging on a heated graphite surface. The proposed model accounts not only for the oxidation reactions typically modeled in the heritage models, but also accounts for the nitridation reactions with formation of the CN molecule and recombination reactions of atomic oxygen and nitrogen.

The thermo-chemical non-equilibrium flow physics is modeled with a near body solver (NBS) within a Cartesian Higher-Order Adaptive Multi-Physics Solver (CHAMPS). The solver is classified as a NBS-Cart solver because the solver behavior resembles an overset grid approach between the NBS and Cartesian solver negating the use of an immersed boundary. The curvilinear near body solver accurately captures the high heating gradients at the surface and the Cartesian solver employs an Adaptive Mesh Refinement (AMR) algorithm to adjust the mesh around a moving shock and disturbances [8–12]. The CHAMPS NBS-Cart solver used in this work has been previously validated using a wall-model coupling to an Cartesian solver for perfect gas and high-enthalpy heat flux predictions in Ref. 13. Additionally the solver was successfully coupled to an array of one-dimensional material response solvers with surface ablation and successfully modeled sublimation of camphor material in hypersonic flow [14].

The material response including heat conduction, surface reactions and mesh motion is modeled using the Kentucky Aerothermodynamics and Thermal Response System designated as KATS-MR.The solver employs an implicit scheme with a first-order accurate solution in time and second-order accurate solution in space. Mesh adaptation for surface ablation is modeled with a recently implemented mesh motion approach using

Radial Basis Functions (RBF) [15]. Performance of the solver was extensively explored in the past for charring ablation problems with pyrolysis gas flow [16] and orthotropic material properties [17]. Additionally, KATS was applied to study spallation problems in arc-jet environments by Davuluri et al. [18] and thermo-structural response problems by Fu et al. [19].

To explore the performance of the developed coupled simulation and the recently proposed air-carbon reaction model we study ablation of graphite from two IHF arc-jet experimental campaigns. The first test case is a high enthalpy, long duration sphere-cone ablation experiment in air initially presented by Chen et al. [20] and later studied by several researchers with various levels of fidelity [2, 21, 22]. This test case was well characterized, including measurements of surface temperature with an infrared camera and pyrometer and measurements of recession at two locations on the nose section. The second test case is a lower enthalpy, short duration iso-q shape ablation experiment in air recently performed at NASA Ames center. Characterization of the experiment included surface temperature measurements by multiple pyrometers, as well as in-depth temperature measurement with thermocouples. Having a negligible amount of recession, this test case provides a valuable data for validation of the temperature response of the material subjected to the arc-jet flow environment.

2 Fluid Governing Equations

In this work the chemically-reactive flow from the arc-jet nozzle interacting with the graphite surface is modeled with an 11-species air-carbon model. The free stream arc-jet flow is modeled with a 5-species air model, consisting of N_2, O_2, NO, N and O species and the air-carbon mixture resulting from the gas-surface reactions and material sublimation adds an additional six species CO_2, CO, CN, C, C_2 and C_3 into the model. The addition of ablation species leads to additional chemical reactions in the boundary layer and also affects the transport properties of the boundary layer gas. The thermal non-equilibrium, resulting from the high temperature gas of the arc-jet flow, is modeled using Park's two-temperature model [23] accounting for the translational-rotational temperature, T, and a vibrational-electronic temperature, T_{ve}. Ionization and radiative effects within the fluid flow field are neglected in this work to reduce the computational cost of the employed gas model. The chemically-reacting flow in thermo-chemical non-equilibrium (TCNE) is modeled using the compressible Navier-Stokes equations as in Eq. (1)

$$\frac{\partial \boldsymbol{U}}{\partial \boldsymbol{P}} \frac{\partial \boldsymbol{P}}{\partial t} + \nabla \cdot \Big(\boldsymbol{F} - \boldsymbol{F_d} \Big) = \boldsymbol{W}, \tag{1}$$

where $\boldsymbol{U}$ is the conservative state vector, $\boldsymbol{P}$ is the primitive state vector, $\boldsymbol{F}$ is the convective flux, $\boldsymbol{F_d}$ is the viscous flux and $\boldsymbol{W}$ is the thermo-chemical source term. Eq. (2) presents the primitive and conservative state vectors, such that ρ_s is the species density, ρ is the total fluid density, $\boldsymbol{V} = (u, v, w)^T$ is the fluid velocity vector with its specified components in the Cartesian reference frame, and E and E_{ve} are the total energy and vibrational-electronic energy components per unit volume

$$\boldsymbol{U} = \begin{Bmatrix} \rho_1 \\ \vdots \\ \rho_s \\ \rho u \\ \rho v \\ \rho w \\ E \\ E_{ve} \end{Bmatrix} \text{ and } \mathrm{P} = \begin{Bmatrix} \rho_1 \\ \vdots \\ \rho_s \\ u \\ v \\ w \\ T \\ T_v \end{Bmatrix}. \tag{2}$$

The convective, viscous, and source term vectors are given in Eq. (3) where p is the mixture pressure, $\boldsymbol{J_s}$ is the mass diffusion flux vector of species s, $\boldsymbol{\tau}$ is the viscous stress tensor, κ_{tr} and κ_{ve} are the fluid conductivities for the translational/rotational and vibrational-electronic energy modes respectively, h_s is the enthalpy of species s, ω_s is the source term for the chemical reactions, S_{t2v} is the source term for the energy exchange between the translational and vibrational energy modes, S_{c2v} is the energy exchange due to chemical reactions, and $\hat{u}$ is defined as the contravariant velocity.

$$\boldsymbol{F} = \begin{Bmatrix} \rho_1 \hat{u} \\ \vdots \\ \rho_s \hat{u} \\ \rho u \hat{u} + p\delta_{1i} \\ \rho v \hat{u} + p\delta_{2i} \\ \rho w \hat{u} + p\delta_{3i} \\ (E+p)\hat{u} \\ E_{ve}\hat{u} \end{Bmatrix}, \boldsymbol{F_v} = \begin{Bmatrix} -\boldsymbol{J_1} \\ \vdots \\ -\boldsymbol{J_s} \\ \boldsymbol{\tau_{1i}} \\ \boldsymbol{\tau_{2i}} \\ \boldsymbol{\tau_{3i}} \\ \kappa_{tr}\boldsymbol{\nabla} T + \kappa_{ve}\boldsymbol{\nabla} T_v - \sum_{s=1}^{ns} \boldsymbol{J_s} h_s + \boldsymbol{\tau V} \\ \kappa_{ve}\boldsymbol{\nabla} T_v - \sum_{s=1}^{ns} \boldsymbol{J_s} e_{ve,s} \end{Bmatrix}, \text{ and } \boldsymbol{W} = \begin{Bmatrix} \omega_1 \\ \vdots \\ \omega_s \\ 0 \\ 0 \\ 0 \\ 0 \\ S_{t2v} + S_{c2v} \end{Bmatrix}. \quad (3)$$

The species viscosity and conductivity properties are computed using Blottner and Eucken models. The mixture viscosity and conductivity are computed with Wilke's mixing rule. The mass diffusion flux is assumed to follow Fick's first law as shown in Eq. (4) where $\boldsymbol{\nabla} Y_s$ is the gradient of the species mass fraction and D_s is the species diffusion coefficient. In this work, the species diffusion coefficients are approximated with a single binary coefficient D at a constant Lewis number, Le of 1.4, where $C_{p,\text{tr}}$ is the mixture translational/rotational specific heat at constant pressure

$$\boldsymbol{I_s} = -\rho D \boldsymbol{\nabla} Y_s, \quad (4)$$

and

$$D = \frac{\text{Le}\kappa_{\text{tr}}}{\rho C_{p,\text{tr}}}. \quad (5)$$

Sutton and Gnoffo (1998) [24] have noted that Fick's law does not guarantee that the mass diffusion fluxes will sum to zero resulting in errors in capturing the correct mass fraction gradients among other errors. Modified Fick's law is used in this work to improve the solution accuracy and is given by

$$\boldsymbol{J_{s \neq e}} = \boldsymbol{I_s} - Y_s \sum_{r \neq e}^{ns} \boldsymbol{I_r}, \quad (6)$$

where e denotes the electron species (not included in this work) since the charge neutrality of the flow-field must be handled separately.

The chemical source term used in this work contains 24 reactions. In the list below, reactions 1-8 model dissociation of each molecular species in the flow-field while reactions 9-24 are exchange reactions. The complete list of reactions being modeled is

1. $N_2 + M \rightleftharpoons N + N + M$
2. $O_2 + M \rightleftharpoons O + O + M$
3. $NO + M \rightleftharpoons N + O + M$
4. $C_3 + M \rightleftharpoons C_2 + C + M$
5. $CO_2 + M \rightleftharpoons CO + O + M$
6. $C_2 + M \rightleftharpoons C + C + M$
7. $CO + M \rightleftharpoons C + O + M$
8. $CN + M \rightleftharpoons C + N + M$
9. $N_2 + O \rightleftharpoons NO + N$
10. $NO + O \rightleftharpoons O_2 + N$
11. $CO + O \rightleftharpoons C + O_2$
12. $CN + O \rightleftharpoons NO + C$
13. $CO_2 + O \rightleftharpoons O_2 + CO$
14. $CO + C \rightleftharpoons C_2 + O$
15. $N_2 + C \rightleftharpoons CN + N$
16. $CN + C \rightleftharpoons C_2 + N$
17. $C_3 + C \rightleftharpoons C_2 + C_2$
18. $CO + N \rightleftharpoons CN + O$
19. $CO + N \rightleftharpoons NO + C$
20. $CO + CO \rightleftharpoons CO_2 + C$
21. $C_2 + CO \rightleftharpoons C_3 + O$
22. $CO + CO \rightleftharpoons C_2 + O_2$
23. $CO + NO \rightleftharpoons CO_2 + N$
24. $N_2 + O_2 \rightleftharpoons NO + NO$

For the chemical source term, $\dot{w}_{sr}$ is the chemical production rate of species s in reaction r and is given by

$$\dot{w}_{sr} = (\nu_{sr}^{''} - \nu_{sr}^{'}) \left[10^3 k_{fr} \prod_{j=1}^{ns} \left(10^{-3} \frac{\rho_j}{M_j} \right)^{\nu_{jr}^{'}} - 10^3 k_{br} \prod_{j=1}^{ns} \left(10^{-3} \frac{\rho_j}{M_j} \right)^{\nu_{jr}^{''}} \right], \tag{7}$$

and the source term, ω_s, by

$$\omega_s = M_s \sum_r \dot{w}_{sr}, \tag{8}$$

where k_{fr} and k_{br} represent the forward and backward reaction rates and $\nu^{'}$ and $\nu^{''}$ are the stoichiometric coefficients for reactants and products, respectively. Further details on the chemical-reaction model as well as the data for the used constants and coefficients can be found in the previous extensive work in Ref. 3.

3 Material Response Solver Framework

POCO graphite used in the experiments is modeled in this study as an impermeable solid with a constant density, isotropic and temperature dependent thermal properties. The thermal response of the material undergoing surface recession due to ablation is modeled using the transient energy equation. In KATS, the transient energy governing equation represented in the Arbitrary Lagrangian-Eulerian frame of reference is shown below

$$\frac{\partial U}{\partial t} - \boldsymbol{\nabla} \cdot (\boldsymbol{F}_d + \boldsymbol{F}_g) = 0, \tag{9}$$

where $U = \rho_s c_{p,s} T$ is the thermal energy storage term, ρ_s is the solid density, $c_{p,s}$ is the solid specific heat and T is the temperature. The next term, $\boldsymbol{F}_d = k_s \boldsymbol{\nabla} T$ is the heat diffusion flux, where k_s is the solid conduction. And the last term $\boldsymbol{F}_g = U \bar{\boldsymbol{\omega}}^{\boldsymbol{T}}$ is the grid advection flux, where $\bar{\boldsymbol{\omega}}$ is the averaged grid face velocity vector given in Eq. (10).

$$\bar{\boldsymbol{\omega}} = \frac{\Delta \bar{V}}{A \Delta t} \mathbf{1}, \tag{10}$$

where $\Delta \bar{V}$ is the averaged facial volumetric increment and A is the face area. More details on the grid flux evaluation scheme can be found in Ref. 25.

Subjected to the surface recession, KATS employs a three-dimensional mesh motion scheme that utilizes radial basis functions to interpolate the displacement of the surface elements to the motion of the nodes in the complete domain. Nodes, located at the free boundaries such as the back wall and the symmetry plane are forced to slide. Motion of the symmetry plane nodes is projected onto the corresponding face element in the direction of the node motion. Interface or back wall nodes, if they are located on a flat surface oriented in one of the Cartesian directions, are incorporated in the RBF interpolation matrix with enforcement of zero displacement in the wall normal direction. This defines a non-penetration condition for the volume nodes in the vicinity of the wall and allows node sliding along the interface. Nodes located at the edges, such as a triangular tip of a two-dimensional slice or the edge are moved using a ghost face approach. The nearest face element with its recession vector is mirrored across the local symmetry plane and the ghost face is included in the interpolation matrix to force the displacement of the edge nodes along the local symmetry axis or plane. More details on the implemented mesh motion algorithm can be found in Ref. 25.

3.1 Physical and Thermal Properties of Graphite

Physical and thermal properties of POCO graphite were obtained from several sources and compared. Touloukian [26, 27] provides properties for POCO graphite for the highest temperature range, covering most of the experimental conditions. Taylor [28] also has quite a large temperature range, however the conductivity and specific heat are limited to 3000 K and emissivity data was not found. Finally, the most recent measurements for several types of graphite were presented by Sheppard et al. [29], including thermal emissivity. Unfortunately the measured temperature range is also quite limited and could not cover the full

expected range of surface and in-depth material temperatures in the simulation. From the comparison of the obtained properties shown in Fig. 1 it is noticeable that all three sources predict comparable values in the common temperature range, except for some differences in the emissivity. Density of POCO graphite obtained from the sources varies between 1660 to 1730 kg/m^3.

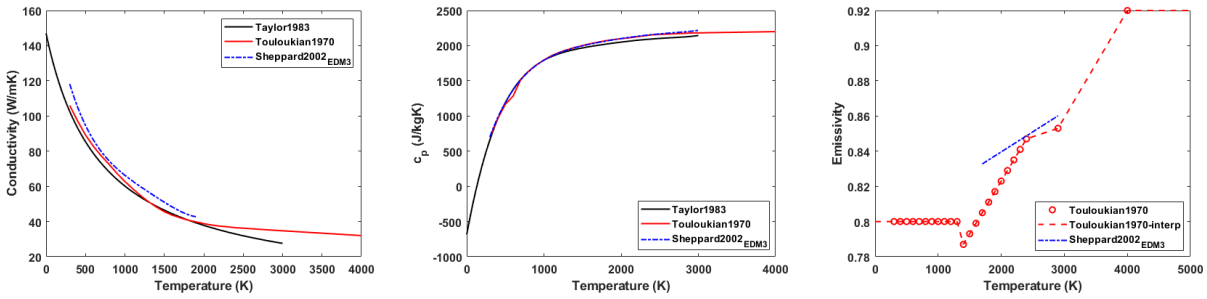

(a) Conductivity (b) Specific heat (c) Surface emissivity

Figure 1: Thermal properties of POCO graphite [26–29].

3.2 Boundary Conditions

In the developed coupled simulation, the surface balance equations are solved as part of the material response solution. This provides additional accuracy when the material temperature response is included in the solution of the surface balance equations. The set of boundary conditions exchanged between the flow and material solvers is obtained from solution of the conservation equations for the mass, momentum, and energy, in addition to the finite-rate surface chemistry model. The state of the gas at the wall is defined with the perfect gas law. The energy balance at the surface is composed of the incident translational-rotational and vibrational conduction fluxes as well as the diffusive species fluxes from the flow side and material conduction, re-radiation and ablation heat flux from the material side. Equation (11) represents the energy balance at the surface

$$\underbrace{-\kappa_{tr}\boldsymbol{\nabla}T\cdot\hat{\boldsymbol{n}}}_{\substack{\text{translational-rotational}\\ \text{energy conduction}}} \underbrace{-\kappa_{ve}\boldsymbol{\nabla}T_v\cdot\hat{\boldsymbol{n}}}_{\substack{\text{vibrational energy}\\ \text{conduction}}} \underbrace{-\sum_{k=1}^{ns}\rho h_k D\boldsymbol{\nabla}Y_k\cdot\hat{\boldsymbol{n}}}_{\text{diffusion heating}} = \underbrace{-\kappa_s\boldsymbol{\nabla}T\cdot\hat{\boldsymbol{n}}}_{\substack{\text{solid energy}\\ \text{conduction}}} \underbrace{+\epsilon\sigma(T_w^4-T_\infty^4)}_{\text{re-radiation}} + \underbrace{m_w''\left(h_w-h_{s,w}\right)}_{\text{ablation flux}}, \tag{11}$$

where on the material side (right), ϵ is the surface emissivity, σ is the Stefan-Boltzmann constant, h_w is the gas enthalpy evaluated at the wall conditions and $h_{s,w}$ is the solid enthalpy at the wall conditions. The energy equation is solved for the solid conduction flux into the material.

The momentum balance at the wall is modeled with a simple one-dimensional wall-normal exchange of the momentum flux at the surface. Equation (12) represents the momentum balance between the near-wall fluid cell and the wall

$$p_\eta = p_f + \rho_f u_f^2 = p_w + \rho_w u_w^2, \tag{12}$$

where p is the bulk gas static pressure and the subscripts "w", "f" and "η" represent wall, flow and net conditions respectively. The thermodynamic state of the gas at the wall is represented by the perfect gas law, which is given by

$$p_w = \rho_w R T_w, \tag{13}$$

where $R = R_u/M$ is the specific gas constant and M is the mixture molecular weight.

By combining the momentum balance equation with the equation of state and the total species blowing flux at the wall, which is provided later, the bulk gas velocity, pressure and density at the wall can be

computed using Eq. (14) as

$$\begin{aligned} u_w &= \frac{2RT_w m''_w}{p_\eta + \sqrt{p_\eta^2 - 4RT_w m''^2_w}}, \\ p_w &= \frac{p_\eta + \sqrt{p_\eta^2 - 4RT_w m''^2_w}}{2} \quad \text{and} \\ \rho_w &= \frac{p_\eta + \sqrt{p_\eta^2 - 4RT_w m''^2_w}}{2RT_w}. \end{aligned} \tag{14}$$

The mass balance at the wall represents a balance between the species fluxes reaching the wall by diffusion and chemical production versus the net species flux advecting away from the wall, referred to as blowing. The mass balance at the wall is given by Eq. (15)

$$\underbrace{-\rho_w D \frac{\partial Y_k}{\partial \eta}}_{\text{diffusion}} + \underbrace{m''_k}_{\text{production}} = \underbrace{m''_w Y_{k,w}}_{\text{blowing}}, \tag{15}$$

where m''_k is the individual species production flux at the wall and m''_w is the net species blowing flux away from the wall, given in Eq. (16). The mass balance equation is solved for the species mass fraction at the wall $Y_{k,w}$.

$$m''_w = \sum_{k=1}^{ns} m''_k. \tag{16}$$

The gas-surface reactions between the carbon material and the air species as well as the sublimation reactions, as a result of the material phase change, represent the thermo-chemical ablation of the graphite. The gas-surface reactions are irreversible and lead to the direct loss of carbon material from the surface. On the other side, sublimation is a reversible process and if the partial pressure of the carbon species at the wall exceeds the vapor pressure, carbon can condense back to the surface.

In this work, the gas-surface reactions are computed using the recently developed air-carbon reaction model, designated as the ACA model by Prata et al. [7]. In this model, reaction probabilities were constructed based on continuous beam experiments where atomic oxygen and nitrogen, as well as molecular oxygen species were directed at the resistively heated vitreous carbon surface at temperatures ranging from 800 to 1873 K. The resultant products, desorbed from the surface, were detected with rotatable mass spectrometers and the relative fluxes of the resultant species were measured. The constructed model consists of 20 reactions, including oxidation with the formation of carbon monoxide and carbon dioxide, nitridation reactions with the production of the cyanogen radical CN, as well as recombination reactions to form molecular oxygen and nitrogen at the surface. The list of the 20 reactions is shown below

1. $O + (s) \rightarrow O(s)$
2. $O(s) \rightarrow O + (s)$
3. $O + O(s) + C(b) \rightarrow CO + O + (s)$
4. $O + O(s) + C(b) \rightarrow CO_2 + (s)$
5. $O + (s) \rightarrow O^*(s)$
6. $O^*(s) \rightarrow O + (s)$
7. $O + O^*(s) + C(b) \rightarrow CO + O + (s)$
8. $O^*(s) + O^*(s) \rightarrow O_2 + 2(s)$
9. $O(s) + O(s) \rightarrow O_2 + 2(s)$
10. $N + (s) \rightarrow N(s)$
11. $N(s) \rightarrow N + (s)$
12. $N + N(s) + C(b) \rightarrow CN + N + (s)$
13. $N + N(s) \rightarrow N_2 + (s)$
14. $N(s) + N(s) \rightarrow N_2 + 2(s)$
15. $N(s) + C(b) \rightarrow CN + (s)$
16. $O_2 + 2(s) \rightarrow 2O(s)$
17. $O_2 + O(s) + C(b) \rightarrow CO + O_2 + (s)$

18. $O_2 + O(s) + C(b) \rightarrow CO_2 + O + (s)$
19. $O_2 + 2(s) \rightarrow 2O^*(s)$
20. $O_2 + O^*(s) + C(b) \rightarrow CO + O_2 + (s)$

The rate equations for each species depend on the surface coverage of available sites where carbon or air species can adsorb to. Details on solution of the system of equations for the surface site density and the rate equations, as well as the rate constants are given in details in the work of Prata et al. [7]. Verification of the model implementation in 0-D simulation, as well as in the coupled mode at steady state surface conditions was verified in the work of McQuaid et al. [3].

Finally, the sublimation reactions are modeled using the Knudsen-Langmuir formulation for non-equilibrium surface evaporation [30]. In this work, three sublimation reactions of carbon are modeled and are shown below

1. $C(b) + (s) \leftrightarrow C + (s)$
2. $2C(b) + 2(s) \leftrightarrow C_2 + 2(s)$
3. $3C(b) + 3(s) \leftrightarrow C_3 + 3(s)$,

where C(b) represents solid carbon atom and (s) represents an available surface bond site. The rates of sublimation/condensation of carbon species are given by the Knudsen-Lagmuir equation as

$$m''_k = \alpha_k \left(p_{v,k} - p_k\right) \sqrt{\frac{M_k}{2\pi R_u T_w}}, \tag{17}$$

where α_k is the experimentally determined vaporization coefficient and $p_{v,k}$ and p_k are the vapor and partial pressures of carbon species k. The vapor pressure of each carbon species is given by

$$p_{v,k} = 101300.0 \exp\left(P_k/T_w + Q_k\right). \tag{18}$$

The values for α_k, P_k and Q_k are given in Table 1.

Table 1: Carbon vapor pressure coefficients [31].

	C	C_2	C_3
α_k	0.14	0.26	0.03
P_k	-85715	-98363	-93227
Q_k	18.69	22.20	23.93

4 Coupling Framework

The coupling between the CHAMPS NBS-Cart and KATS-MR has been developed to be very efficient for large scale problems with moving and not necessarily aligned interfaces. The coupling is performed in a modular way where the solution of each solver is exchanged through a mutually shared library that collects and transfers the local boundary data structures between the solvers. Schematics of the coupling framework as well as the major solution modules in each solver is shown in Fig. 2. The coupled simulation starts by applying boundary conditions from the converged base flow solution on the material surface. KATS solves first, iteratively, the surface balance equations using the flow boundary conditions and surface temperature taken from the previous step. The solution of the balance equations updates the surface state and recession. The computed ablation energy flux along with the flow heat flux is fed into the energy balance equation to compute the conductive flux into the material. In addition, mesh motion due to the surface recession induces grid fluxes that are computed and also fed into the transient energy equation. The complete set of the updated boundary conditions, including surface temperature, species partial density, blowing velocity and recession of each face is transferred then through the coupling interface to the NBS solver.

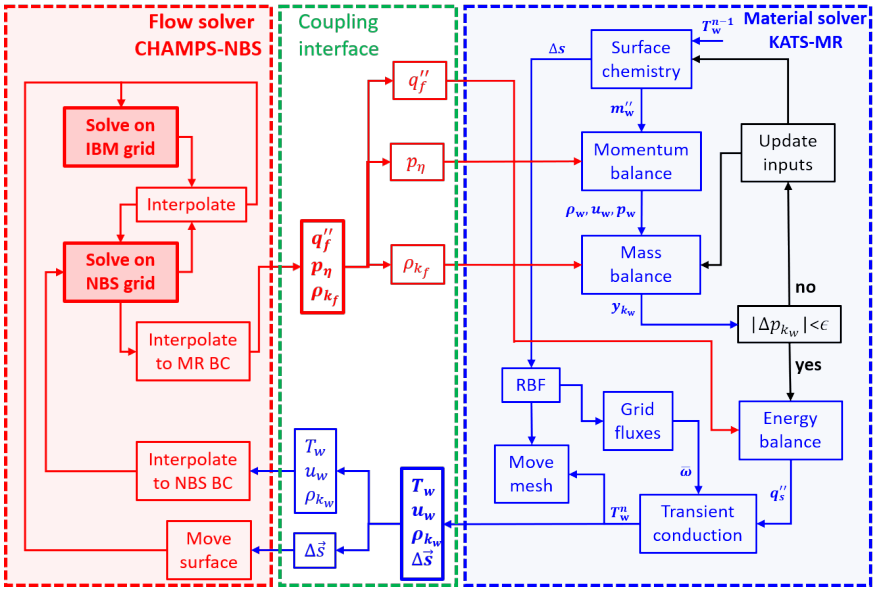

Figure 2: CHAMPS-KATS coupling scheme.

The NBS solver regenerates the near body mesh based on the applied surface recession. It then applies the material boundary conditions and copies the previous step flow solution into the displaced grid. The NBS takes advantage of the structured wall-normal grid layout to employ a line implicit Gauss-Seidel solver to allow for efficient time integration for both steady and unsteady flow simulations. The NBS solves the full set of Navier-Stokes equations to remain consistent with the Cartesian grid solution. This numerical formulation yields accurate boundary layer profiles at computational expenses that are significantly reduced versus a fully-resolved IBM solution and more comparable to the cost of a traditional body-fitted grid approach. Solution of the NBS solver is transferred then to the Cartesian region via the overset interpolation and the off-body flow field solution, as well as the refinement around the shock layer is updated.

Mapping of the non-conformal grid solutions between the solvers is performed by utilizing K-d trees that are used to identify n-nearest points to each surface centroid and build an interpolation cloud. From the assembled point cloud, coefficients for the interpolation polynomials are computed and stored. This process is performed on the NBS surface partition because the KATS partition does not guarantee optimal load balancing of the surface points whereas the NBS is solved in a sequential manner to the Cartesian grid solver and so its partition exists equally across all processors.

Since grids on the material and NBS surfaces are generated independently the coupled solution allows for a mismatch between the face elements. The mismatched surface elements may lead to interpolation errors due to significant surface recession. To treat this issue, the interpolation point is projected onto the line segment connecting the two nearest points within its own interpolation cloud. This modified point coordinate is then used to generate the interpolating polynomial coefficients. More details on the implemented interpolation procedure as well as the mapping performed between the three solvers can be found in previous work [3, 6].

5 Simulation results and discussion

The developed coupled interaction between the two solvers was applied to study graphite material ablation in the arc-jet flow environment. The first test case is a sphere-cone graphite model tested in air in the IHF arc-jet facility at NASA Ames Research Center. The estimated bulk enthalpy is 27 MJ/kg, with stagnation heat flux of 2100 W/cm^2 and stagnation pressure of 0.80 atm. At these conditions, nitrogen gas is partially dissociated and oxygen is fully dissociated. The geometry of the model is a 10° half-angle sphere cone with nose radius of 1.905 cm and length of 8.89 cm. In the current study, the overall length of the model was trimmed to 5 cm to reduce the computational cost of the simulation. The geometry of the simulated model is shown in Fig. 3(a). The simulation conditions for this case were obtained from Ref. 2 and are shown in

Table 2 for case 1. The total duration of the experiment is 30 sec and as mentioned by the author, the back wall of the model was connected to a water cooled holder and is assumed to be at a constant temperature of 312 K. The experimental measurements in this test included pyrometer and infrared camera at 45° location, as well as measurement of recession at multiple time instants at 0° and 45° locations. This test case uses thermal properties from Touloukian [26], Touloukian and DeWitt [27] and a solid density of 1730 kg/m^3 as was reported by the reference study Chen et al. [20].

The second test case is an iso-q graphite model tested in air the IHF arc-jet facility at NASA Ames as a part of larger experimental campaign, where analysis of additional test cases can be found in the work of Askins et al. [32]. The estimated bulk enthalpy is 20.7 MJ/kg, with stagnation heat flux of 1306 W/cm^2 and total pressure of 127.3 kPa. The measurement of the heat flux and pressure values were made with a hemispherical calorimeter with 2-in diameter. The experimental graphite model is a 4-in iso-q shape as shown in Fig. 3(b). As it can be seen, the measurement probe and the graphite sample were of different dimensions and hence, comparison of the simulated and measured heat flux and pressure values should be done mindfully. The back wall of the graphite model was insulated with LI-2200 and was assumed adiabatic in this study. To perform the coupled analysis, first a full arc-jet simulation of this case was performed using DPLR code and then, the free-stream conditions for the coupled simulation were sampled at the centerline before the shock location. These conditions are shown in Table 2 for case 2. The experiment included around 7 % of the Argon gas. It should be mentioned, that in our study we have not included Argon as a flow species and assumed that the mass fraction of the gas is distributed proportionally between all other species. These conditions are designated in the table as case 2 - adj. Exclusion of Argon from the simulation and redistribution of the mass between other species resulted in some change of the enthalpy of the species. From the conducted analysis using Mutation++ thermochemistry library [33] the original species enthalpy was 7.33 MJ/kg and after the exclusion of Argon and redistribution of the mass, the enthalpy became 7.76 MJ/kg. The difference in the enthalpies could potentially introduce some inaccuracy in the surface conditions. This effect was not quantified in the current study. The experimental measurements in this test included pyrometer and five thermocouples distributed on the stagnation line at different depths as shown in Fig. 3(b). The material used in the experiment was ultra-fine POCO-graphite EDM3 and the thermophysical properties used here were taken from Sheppard et al. [29].

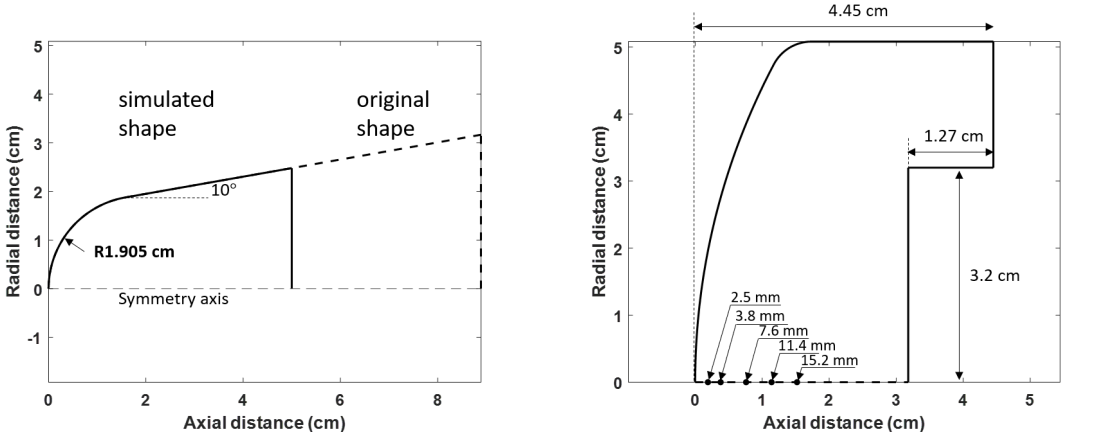

(a) Case 1 - sphere-cone shape.

(b) Case 2 - iso-q shape and thermocouple locations.

Figure 3: Simulated geometries for case 1 and case 2.

The simulation of a chemically reactive flow in thermochemical non-equilibrium is computationally expensive. In addition, adapting the flow solution to the recessing wall increases the time it requires for the flow solution to re-converge. The performed simulations were set as follows. At the wall, a grid spacing of 1×10^{-6} m was used in both domains. The NBS uses an unsteady line implicit solver to adequately converge the boundary layer solution within each time step. To increase the speed of the coupled solution and maintain a decent level of accuracy, we employed a hybrid approach to step the solvers. First, both solvers advance in time at the same CFL of 10,000, while the NBS performs additional sub-steps within every given

time step to re-converge the solution in the boundary layer and to maintain time accuracy. Following this tight approach that intends to smooth the initial steep gradient at the wall, the material solver increases its own local time step and advances faster in time than the flow solver. The NBS solver keeps stepping at the same CFL and performs sub-iterations after every exchange of the boundary conditions with KATS. In this setup, we were able to significantly decrease the overall time required to accomplish the full duration of the simulation. It should be mentioned, that fully re-converging the flow solution after each exchange of the boundary conditions is also a costly task and a trade off was made to keep a reasonable number of NBS sub-steps and allow efficient advancement of the coupled solution.

Table 2: Simulation conditions for case 1 from Chen and Milos [2] and case 2 from DPLR simulation.

	Case 1	**Case 2**	**Case 2 - adj**
V (m/s)	5354	4327.4	same
ρ (kg/m^3)	3.0×10^{-3}	7.63×10^{-3}	same
T_{tr} (K)	1428	3812.44	same
T_v (K)	1428	4035.04	same
Y_{N_2}	0.6169	0.6317	0.6828
Y_{O_2}	0.0	3.0191×10^{-5}	3.2637×10^{-5}
Y_{NO}	4.6×10^{-3}	4.437×10^{-4}	4.797×10^{-4}
Y_N	0.1212	0.07617	0.08234
Y_O	0.2573	0.2167	0.23426
Y_{Ar}	0.0	7.494×10^{-2}	0
Duration (sec)	30	5.5	same
T_0 (K)	312	300	same
T_∞ (K)	300	300	same
T_{bw} (K)	312	adiabatic	same

5.1 Case 1 - sphere-cone, high heating

The first arc-jet case is a high enthalpy case with a measured heat flux of 2100 W/cm^2 and stagnation pressure of 0.80 atm. A visualization of the flow-field and material temperature at 0 and 30 sec is shown in Fig. 4. The maximum temperature reached by the flow is 12,660 K in the shock region and material maximum temperature by the end of 30 sec is 3680 K. The long duration of the test combined with the high heat flux has lead to a significant amount of recession and displacement of the shock layer. By the end of 30 sec, the shock is seen further away from the wall due to the blunter shape of the nose.

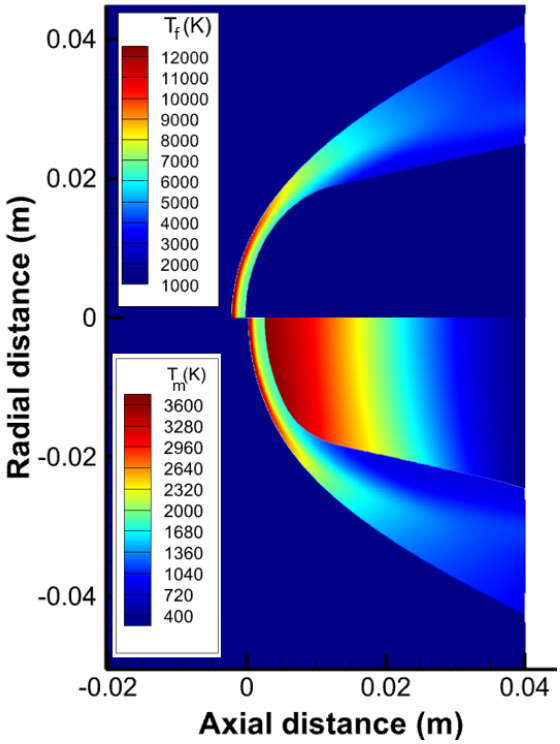

Figure 4: Case 1 - Flow and material temperature contours at 0 and 30 sec (on different scales).

Figure 5(a) shows the evolution of the heat flux at the surface sampled every 3 sec along the duration of the simulation. Reaching the maximum of almost 1900 W/cm^2 at the stagnation point at the beginning of the simulation and decreasing to around 1200 W/cm^2 by the end of 30 sec. It should be noted that the simulated cold wall heat flux was lower than the measured one in the experiment of 2100 W/cm^2. Chen in his study, Ref. 20, also mentions this difference between the predicted and measured heat flux and attributes it to the uncertainty in the estimation of the arc-jet free-stream and material conditions. In our simulation, we assumed the predicted heat flux as the baseline value. From the time evolution of the heat flux it can be seen that the surface conditions and the shape of the model, shown in Fig. 5(d), leads to a quite interesting flattening of the heat flux profile in the nose region. The pressure distribution history is shown in Fig. 5(b). At the stagnation point, the initial pressure matches very closely to the measured 0.8 atm value, presented in Ref. 2. A small increase in the stagnation point pressure can be seen in the figure and is likely attributed to the massive blowing of the ablation products into the boundary layer. Away from the stagnation point, the pressure adjusts to the changing shape of the model, increasing in the more blunt region of the nose and decreasing downstream. The change in the shape of the pressure profile in the nose region is less strong than of the heat flux, implying that the shape change of the nose was probably not the only effect leading to a flattened heat flux profile and will be explored more later.

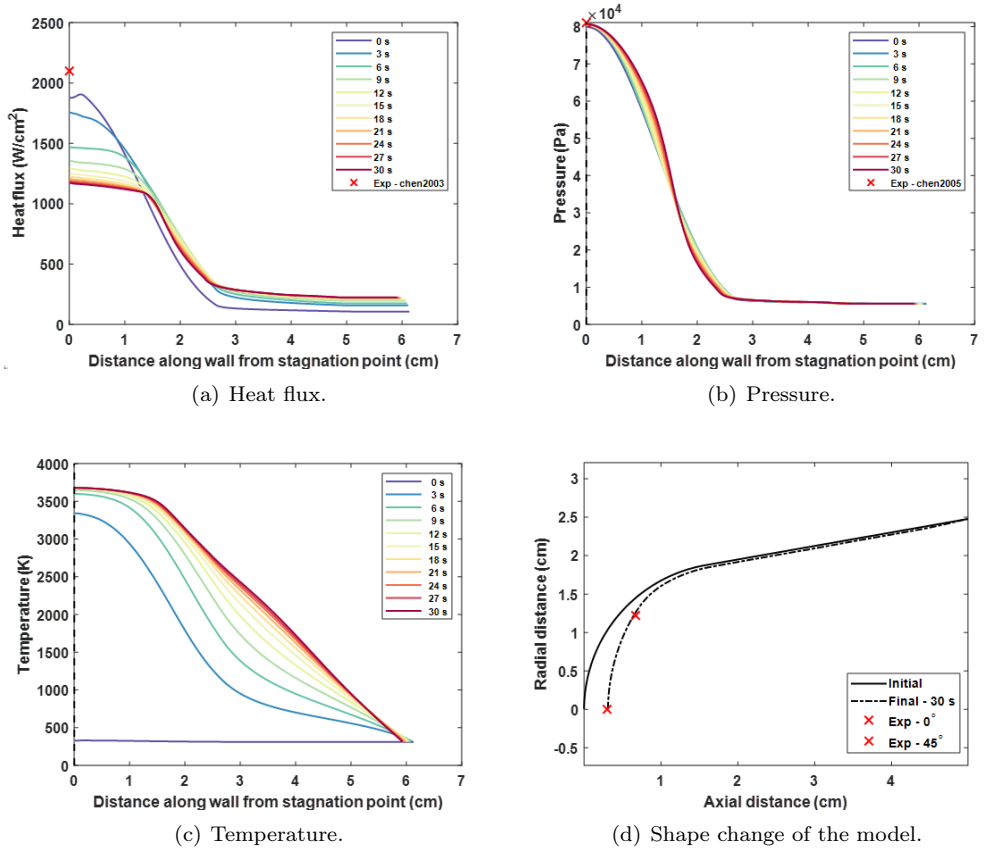

(a) Heat flux.

(b) Pressure.

(c) Temperature.

(d) Shape change of the model.

Figure 5: Case 1 - Distribution and time evolution of surface quantities and shape change of the model.

Figure 6 shows the detailed comparison of the predicted temperature and recession to the measured experimental values. Figure 6(a) shows the predicted time history of the surface temperature at 45° location relative to the stagnation point. The predicted time evolution overestimates the measured value by the IR camera at the end of 30 sec by 250 K. Overestimation of around 150 K is predicted by the coupled simulation of GIANTS-TITAN, that modeled the ablation physics at the wall using the heritage thermochemical equilibrium Bprime approach. The sensitivity of the temperature measurement can be seen from plotting the temperature at $-5°$ and $+5°$ degrees relative to the nominal location. A slightly higher angle of the sampling leads to visible decrease in the temperature, implying that averaging occurring in the measurement spot by pyrometer or IR camera would lead to uncertainty in the accuracy of the local measurement. Figure 6(b) shows the comparison between the predicted and measured recession at 0° and 45°. Stagnation point recession closely follows the experimental curve and most likely stays within the experimental uncertainties of the measurement. Recession at the 45° location is slightly underpredicted compared to both the experimental and numerical reference results, but still stays within a fraction of a millimeter accuracy.

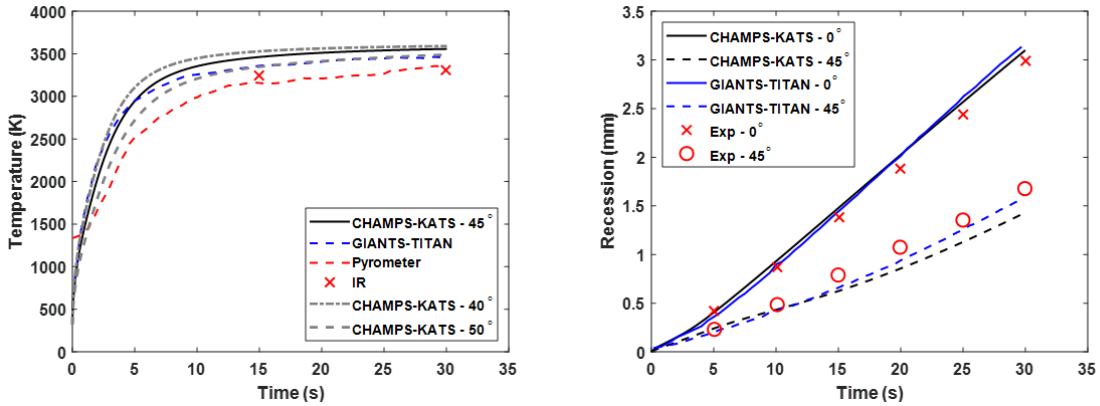

(a) Surface temperature at 45° location relative to stagnation point.

(b) Surface recession at 0° and 45° location relative to stagnation point.

Figure 6: Case 1 - Comparison of predicted and measured surface temperature and recession.

Figure 7(a) shows the distribution of species blowing fluxes along the surface and the total blowing flux, sampled at 30 sec. It can be seen that the major ablation product at the stagnation region is the sublimation species C_3 and the oxidation species CO, with some contribution of sublimation species C_2. Noticeably, atomic carbon species C is condensing to the surface. It happens as a result of dissociation of the carbon bearing species present in the flow and leads to an increase in the partial pressure of carbon at the wall. Away from the stagnation point the oxidation flux of CO species reaches the maximum and gradually decreases toward the back wall. Interestingly, downstream along the conical section CO production shows two distinct local peaks with corresponding two local dips in O consumption. Appearance of the last local peak in CO production should be taken carefully, as in the region beyond 5 cm the flow boundary conditions were imposed artificially as being outside of the physical domain. This behavior is illustrated in Fig. 12(b) in the species mass fractions plot. Behavior of the CO production peaks in the physical domain could be related to prediction of the ACA reaction model that predicts a peak in CO production as a function of the local flux of oxygen atoms [7]. At higher oxygen fluxes the peak in CO production shifts toward higher temperatures. It could interesting to explore further this phenomena. Another significant blowing species at the wall is the molecular nitrogen that recombines or desorbes from the wall, contributing to the catalytic heat flux at the surface. Finally, we observe a very small amount of CN molecules blowing from the surface and most of the nitrogen atoms recombine at the surface and form N_2 molecules.

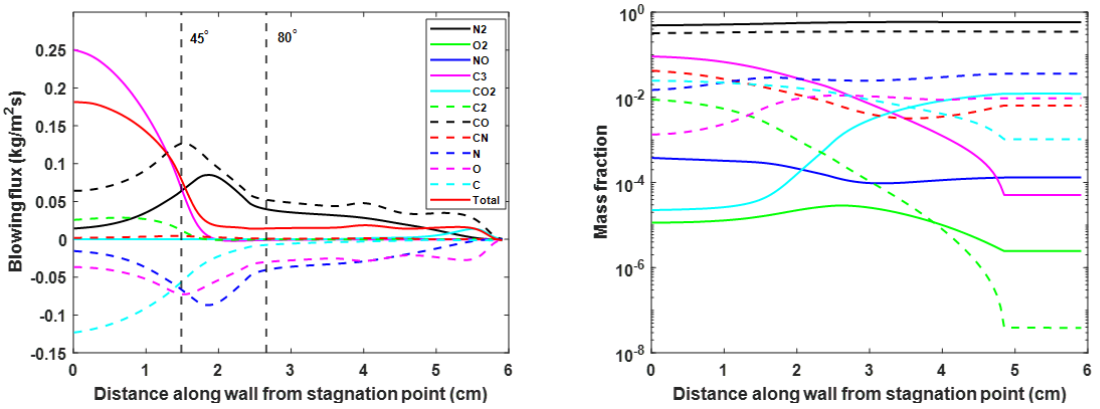

(a) Species blowing fluxes.

(b) Species mass fractions.

Figure 7: Case 1 - Mass blowing and chemical species distribution along the surface at 30 sec.

5.2 Case 2 - iso-q model, lower heating

The second case studied here is the graphite iso-q model, tested for 5.5 sec in arc-jet flow with a bulk enthalpy of 19.8 MJ/kg. Figure 8 shows the temperature contours for the flow and material regions. The maximum flow temperature reaches 10,517 K in the shock layer, while the material maximum temperature is 2290 K by the end of 5.5 sec. The measured recession in this experiment was only a fraction of a millimeter and hence no visible change in the shock location or surface is seen in the figure.

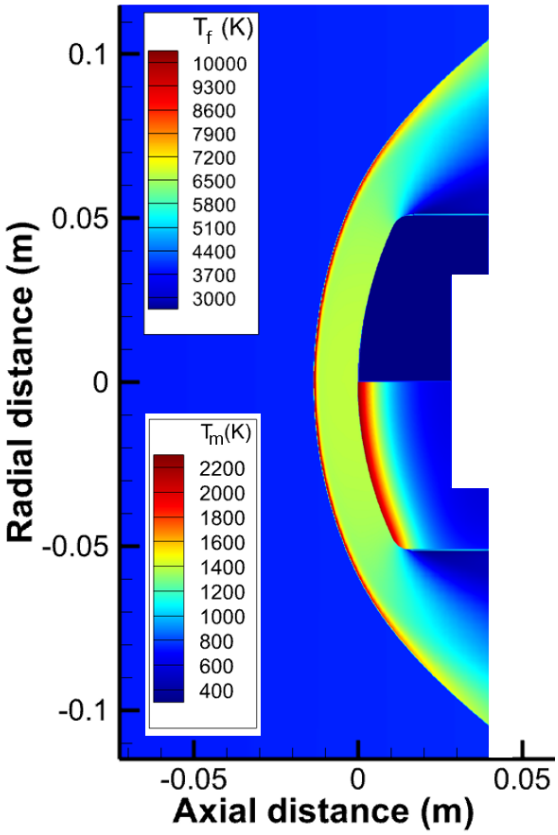

Figure 8: Case 2 - Flow and material temperature contours at 0 and 5.5sec (on different scales).

Figure 9(a) shows the spatial distribution of the heat flux and its time evolution along the simulation. Starting at around 1000 W/cm^2 at the stagnation point, the hear flux gradually decreases and spikes at transition region between the top of the spherical surface and the shoulder. Beyond that point, the heat flux rapidly decreases and reaches approximately a constant value. The geometry of the iso-q model was designed to provide a relatively constant heat flux at the top surface. In general, as the material recesses, the shape of the heat flux is expected to be preserved and even become more uniform. As was predicted in the previous work, Ref 6, the spike at the shoulder region is gradually smoothed as a result of the local topology change and the uniform heat flux even extends further into the shoulder region. The pressure behavior at the surface shown in Fig. 9(b) stays unchanged, with a small increase potentially caused by the blowing gases. Finally, it is observed that the temperature shown in Fig. 9(c) does not reach a steady value by the end of 5.5 sec simulation and keeps gradually increasing. The temperature range indicates that material ablation occurs completely in the oxidation regime.

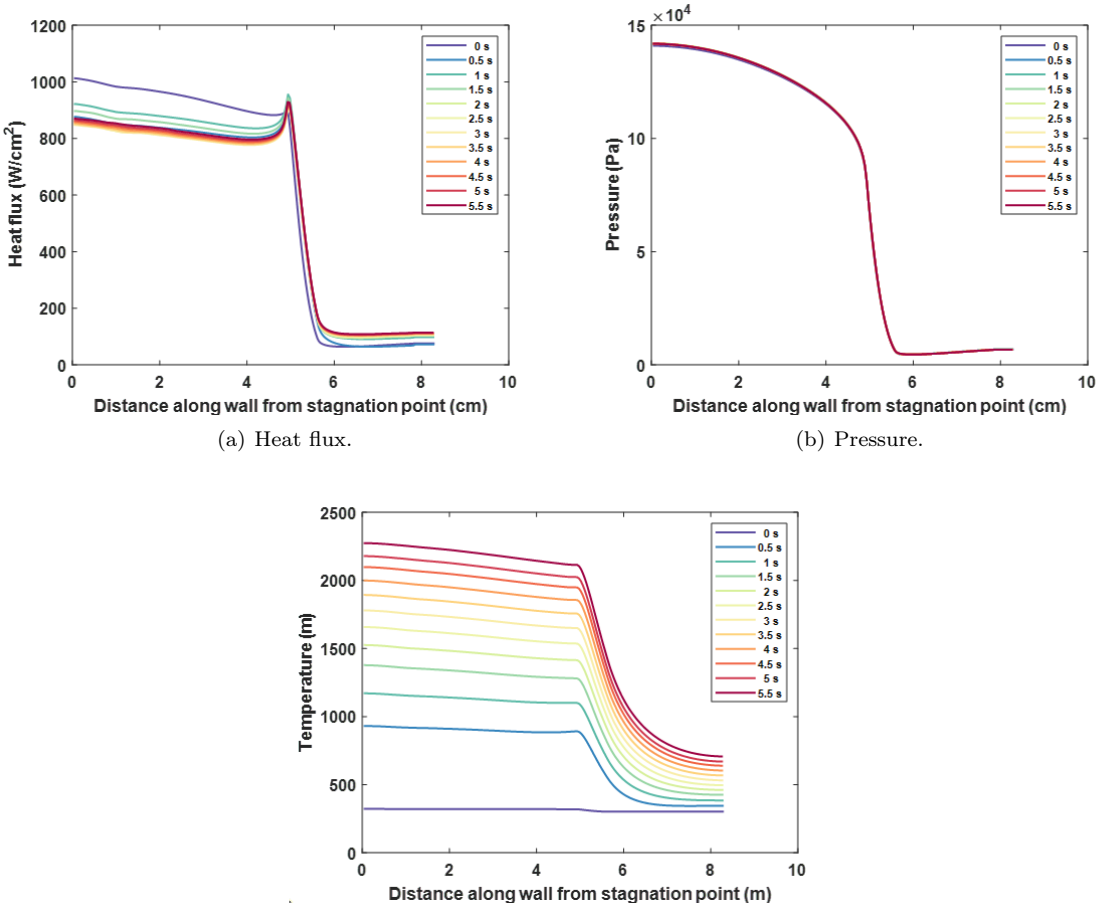

(a) Heat flux.

(b) Pressure.

(c) Wall temperature.

Figure 9: Case 2 - Distribution and time evolution of surface quantities.

The experimental measurements in this test included a set of pyrometers and a plug with five embedded thermocouples at different depths. The analysis of the thermal response of the material was performed with a number of simulations. First, an uncoupled material simulation was performed with an applied aerodynamic heating and pressure conditions extracted from the flow simulation. Since the shape change of the material is minimal in the current test, the change in the heat flux is dictated solely by the local material temperature and gas composition. Using the pre-generated equilibrium thermochemistry tables at a range of temperature and pressure conditions at the wall material simulation was performed. Figure 10(a) shows the predicted surface and in-depth temperature response of the material, depicted with solid lines. The dashed lines represent the measured temperatures from the pyrometer and thermocouples. Quite significant deviation of the predicted temperature can be seen in the results. The shape of the surface temperature is different from the measured one with the pyrometer. The in-depth temperatures are consistently over-predicted, but follow the general shape of the curves.

To explore the reason in the deviation of the predicted results, a TC-driver approach was applied to eliminate the uncertainty in the boundary conditions. The TC-driver approach uses the temperature of the first thermocouple as a boundary condition in the material simulation. In this approach, a 1D simulation is performed, while the length of the material is reduced such that the temperature from the first thermocouple is applied at the surface. The approach simulates a pure conduction problem, with no material ablation or re-radiation. In this case, if the material properties are correct, the in-depth temperature prediction should follow the measured temperatures by the thermocouples. The temperature response of the material during the 5.5 sec heating, followed by 15 sec cooling phase is shown in Fig. 10(b). The first red curve represents the applied temperature from the thermocouple measurement. The predicted temperatures follow

very closely to the measured ones, with small deviation in the deeper locations that most likely related to the two-dimensional conduction effects at this depth. The good agreement of the results indicates that the thermophysical properties in the model are correct and the deviation of the predicted results in the uncoupled simulation is most likely due to the inaccurate boundary conditions and/or surface ablation thermochemistry.

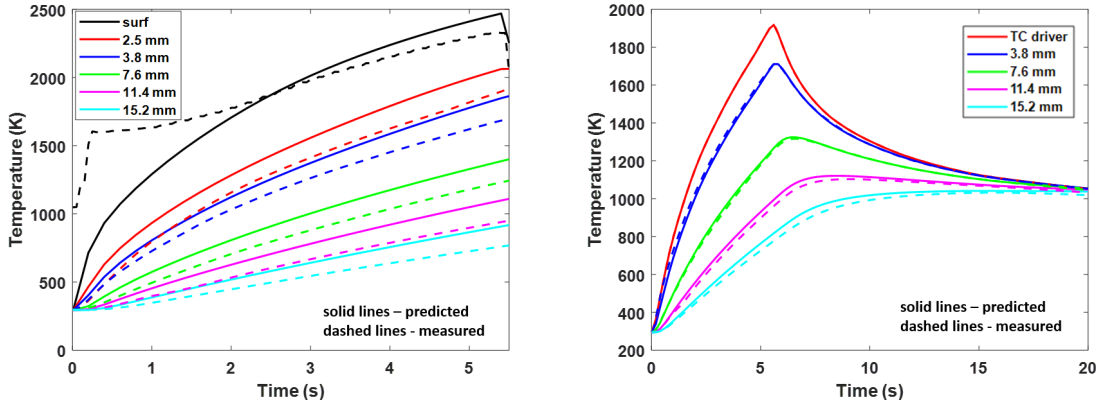

(a) Uncoupled material solution.

(b) One-dimensional TC-driver approach.

Figure 10: Case 2 - Uncoupled simulation and verification of material properties with TC driver approach.

Following the performed analysis, a fully-coupled simulation was performed. Figure 11 shows the predicted temperature response and comparison to the experimental measurements. The predicted surface temperature is somewhat lower than the measured one by the pyrometer, but follows approximately a similar curve after the initial transient. The in-depth temperatures show much closer agreement with the reference data, with much better match at the more shallow locations. A noticeable difference is seen in the shape of the curves in the first second of the simulation, as the predicted temperatures have a stepper curve than the measured one. At the initial transient in the experiment, the surface experiences the highest heating rate and accuracy of the temperature prediction could be affected by the coupling scheme. Time-accurate stepping of the two solvers during the initial transient and longer sub-iterations could help to capture better the thermal response of the material.

The fact that the coupled simulation has predicted more accurately the thermal response of the material than the uncoupled simulation indicates on some differences present in the conduction heat flux into the material that controls the in-depth temperatures. The conductive flux is defined by the balance between the conduction and species diffusion flux incident from the flow and material ablation flux and re-radiation leaving the surface. Given that the initial heat flux to the surface is the same in the uncoupled and coupled simulations, further dynamics of the incident heat flux is determined by the surface temperature and gas composition. The gas composition and surface temperature also drives the ablation heat flux. This implies that the difference in the obtained temperature results could be due to the deviation from the equilibrium conditions at the wall in the coupled simulation. Further analysis will be carried out in the future studies to quantify the differences in the quantities in the boundary layer between the coupled and uncoupled simulations.

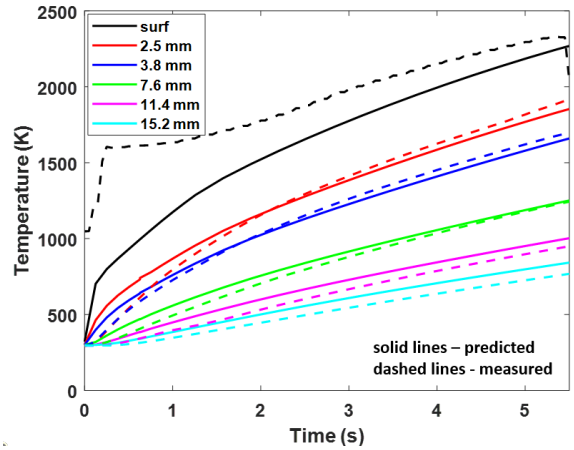

Figure 11: Case 2 - Coupled simulation.

Finally, Fig. 12 shows the distribution of species blowing and mass fractions along the material surface after 5.5 sec of the simulation. It can be seen in Fig. 12(a) that the dominant blowing species is the carbon monoxide, indicating the strong oxidation regime of the material. Significant recombination of nitrogen atoms occurs at the surface with very little production of cyano radical CN. As it was expected, no visible phase change of the material occurs at this temperature. Overall, due to the relatively constant surface heat flux and temperature, the species blowing also follows a uniform shape with a spike in the shoulder region.

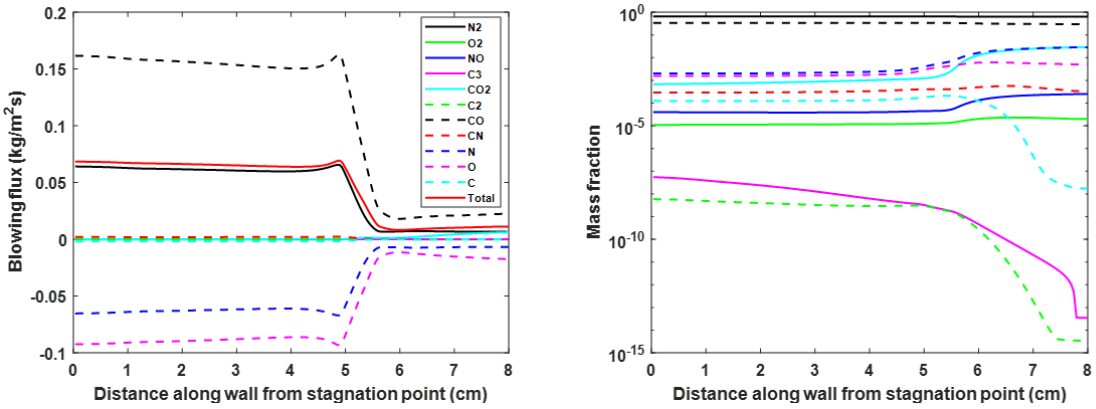

(a) Species blowing fluxes.

(b) Species mass fractions.

Figure 12: Case 2 - Mass blowing and chemical species distribution along the surface at 5.5 sec.

6 Conclusions

In this study we developed a fully-coupled simulation capability between a chemically reacting hypersonic flow and material response solver with a moving wall. The hypersonic flow was simulated with CHAMPS NBS-Cart, efficiently resolving the boundary layer region with a curvilinear near body solver and the off-body region with a block-structure Cartesian grid solver. The material response was simulated with the KATS-MR solver that included a recently developed air-carbon ablation model. The coupled simulation included the full exchange of boundary conditions and iterative solution of the conservation equations on the material side. Accurate adaptation of the flow to the recessing surface was possible due to the use of adaptive mesh refinement technique in the Cartesian region to track the shock and regeneration of the near body mesh as the surface recessed. The developed simulation was applied to study ablation of graphite

tested in arc-jet environment. In the first, highest heating case, the material reached a strong sublimation regime in the nose section, while downstream of the nose oxidation reactions dominated the surface ablation. Prediction of the surface recession was in very good agreement with the experimental results, pointing at the level of maturity of the recently developed finite-rate air-carbon ablation model. Validation of the temperature response of the material was performed using thermocouple data from the second, lower heating case, showing satisfactory agreement with the experimental data. The performed uncoupled simulation of the problem indicated a significant deviation in the predicted temperatures. To localize the source of inaccuracy, a TC-driver approach analysis of the problem was performed. The analysis confirmed the accuracy of the thermophysical properties of POCO graphite used in the simulation and indicated that there is likely differences in the surface thermochemistry conditions between the equilibrium and finite-rate solutions. The performed coupled simulation of the problem highlighted the need for accurate modeling of the boundary layer chemistry to accurately predict the temperature response of the material.

Acknowledgments

The authors would like to recognize and show appreciation for the financial support provided by NASA Kentucky EPSCoR RA Award no. 80NSSC19M0144 (E. Stern technical monitor) and NASA EPSCoR R3 Award no. 80NSSC19M0084 (M. Barnhardt technical monitor).

References

[1] Yih-Kanq Chen, Frank S Milos, and Tahir Gokcen. Loosely coupled simulation for two-dimensional ablation and shape change. *Journal of Spacecraft and Rockets*, 47(5):775–785, 2010. doi: https://doi.org/10.2514/1.39667.

[2] Yih-Kanq Chen and Frank S Milos. Navier-stokes solutions with finite rate ablation for planetary mission earth reentries. *Journal of Spacecraft and Rockets*, 42(6):961–970, 2005. doi: https://doi.org/10.2514/1.12248.

[3] Joel A. McQuaid, Aleksander L. Zibitsker, Alexandre Martin, and Christoph Brehm. Simulation of graphite ablation using an overset near body solver on an adaptive block-structured cartesian off-body grid. In *AIAA Aviation Forum*. AIAA, June 2022. doi: https://doi.org/10.2514/6.2022-4088.

[4] Chul Park. Effects of atomic oxygen on graphite ablation. *AIAA Journal*, 14:1640–1642, 1976. doi: 10.2514/3.7267.

[5] Sergey V Zhluktov and Takashi Abe. Viscous shock-layer simulation of airflow past ablating blunt body with carbon surface. *Journal of thermophysics and heat transfer*, 13(1):50–59, 1999. doi: https://doi.org/10.2514/2.6400.

[6] Aleksander L. Zibitsker, Joel A. McQuaid, Christoph Brehm, and Alexandre Martin. Study of a two-dimensional shape change of blunt-body geometries at hypersonic conditions using fully-coupled simulation. In *AIAA Aviation Forum*. American Institute of Aeronautics and Astronautics, June 2022. doi: https://doi.org/10.2514/6.2022-4006.

[7] Krishna Sandeep Prata, Thomas E Schwartzentruber, and Timothy K Minton. Air-carbon ablation model for hypersonic flight from molecular-beam data. *AIAA Journal*, 60(2):627–640, 2022. doi: 10.2514/1.J060516.

[8] Christoph Brehm and Hermann F Fasel. A novel concept for the design of immersed interface methods. *Journal of Computational Physics*, 242:234–267, 2013. doi: 10.1016/j.jcp.2013.01.027.

[9] Christoph. Brehm, Christoph. Hader, and Hermann . F. Fasel. A locally stablilized immersed boundary method for the compressible navier-stokes equations. *Journal of Computational Physics*, 295:475–504, 2015. doi: 10.1016/j.jcp.2015.04.023.

[10] Christoph Brehm. On consistent boundary closures for compact finite-difference weno schemes. *Journal of Computational Physics*, 334:573–581, 2017. doi: 10.1016/j.jcp.2016.12.057.

[11] Christoph Brehm, M. F. Barad, and C. C. Kiris. Development of immersed boundary computational aeroacoustic predication capabilities for open-rotor noise. *Journal of Computational Physics*, 388:690–716, 2019. doi: 10.1016/j.jcp.2019.02.011.

[12] Jonathan Boustani, Michael F. Barad, Cetin C. Kiris, and Christoph Brehm. An immersed boundary fluid–structure interaction method for thin, highly compliant shell structures. *Journal of Computational Physics*, 438:110369, 2021. ISSN 0021-9991. doi: 10.1016/j.jcp.2021.110369.

[13] Joel A. McQuaid, Aleksander L. Zibitsker, Alexandre Martin, and Christoph Brehm. Heat flux predictions for high speed flows with an immersed boundary method. In *AIAA Aviation Forum*. American Institute of Aeronautics and Astronautics, August 2021. doi: 10.2514/6.2021-3145.

[14] Aleksander L Zibitsker, Joel McQuaid, Christoph Brehm, and Alexandre Martin. Fully-coupled simulation of low temperature ablator and hypersonic flow solver. In *AIAA SCITECH 2022 Forum*, page 0676, 2022. doi: https://doi.org/10.2514/6.2022-0676.

[15] Aleksander L. Zibitsker, Joel A. McQuaid, Christoph Brehm, and Alexandre Martin. Development and verification of a mesh deformation scheme for a three dimensional ablative material solver. In *AIAA Science and Technology Forum and Exposition 2022*. American Institute of Aeronautics and Astronautics, Jan 2022. doi: 10.2514/6.2022-1285.

[16] Haoyue Weng and Alexandre Martin. Multidimensional modeling of pyrolysis gas transport inside charring ablative materials. *Journal of Thermophysics and Heat Transfer*, 28(4):583–597, 2014. doi: https://doi.org/10.2514/1.T4434.

[17] Haoyue Weng and Alexandre Martin. Numerical investigation of pyrolysis gas blowing pattern and thermal response using orthotropic charring ablative material. In *11th AIAA/ASME Joint Thermophysics and Heat Transfer Conference*. AIAA, 6 2014. doi: 10.2514/6.2014-2121.

[18] Raghava Davuluri, Sean Bailey, Kaveh Tagavi, and Alexandre Martin. Numerical reconstruction of spalled particle trajectories in an arc-jet environment. In *AIAA Science and Technology Forum and Exposition*, page 1172, 2021. doi: 10.2514/6.2021-1172.

[19] Rui Fu, Haoyue Weng, Jonathan F Wenk, and Alexandre Martin. Thermomechanical coupling for charring ablators. *Journal of Thermophysics and Heat Transfer*, 32(2):369–379, 2018. doi: https://doi.org/10.2514/1.T5194.

[20] Yih-Kanq Chen, Frank Milos, Dan Reda, and Dave Stewart. Graphite ablation and thermal response simulation under arc-jet flow conditions. In *36th AIAA Thermophysics Conference*, page 4042, 2003. doi: https://doi.org/10.2514/6.2003-4042.

[21] Daniele Bianchi, Francesco Nasuti, and Emanuele Martelli. Navier-stokes simulations of hypersonic flows with coupled graphite ablation. *Journal of Spacecraft and Rockets*, 47(4):554–562, 2010. doi: https://doi.org/10.2514/1.47995.

[22] Charles J Bersbach, Jeremy Evans, Hicham Alkandry, Mark E Ewing, and Daron A Isaac. Ablative thermal response numerical modeling under arcjet test conditions. *Journal of Thermophysics and Heat Transfer*, pages 1–10, 2022. doi: https://doi.org/10.2514/1.T6346.

[23] Chul Park. Assessment of two-temperature kinetic model for ionizing air. *Journal of Thermophysics and Heat Transfer*, 3:233–244, 1989. doi: 10.2514/3.28771.

[24] Kenneth Sutton and Peter A. Gnoffo. Multi-component diffusion with application to computational aerothermodynamics. In *7th AIAA/ASME Joint Thermophysics and Heat Transfer Conference*. AIAA, June 1998. doi: 10.2514/6.1998-2575.

[25] Aleksander L Zibitsker, Joel McQuaid, Christoph Brehm, and Alexandre Martin. Development and verification of a mesh deformation scheme for a three dimensional ablative material solver. In *AIAA SCITECH 2022 Forum*, page 1285, 2022. doi: https://doi.org/10.2514/6.2022-1285.

[26] Y. Sarkis Touloukian. Thermal conductivity, nonmetallic solids. *Thermophys. Properties of Matter*, 2: 183–193, 1970.

[27] Y. Sarkis Touloukian and D. P. DeWitt. Thermophysical properties of matter-the tprc data series. volume 8. thermal radiative properties-nonmetallic solids. Technical report, Thermophysical and electronic properties information analysis center., 1972.

[28] R Taylor. Thermal diffusivity of poco graphite and stainless steel srm 735-s. *Thermal Conductivity 17*, pages 753–762, 1983.

[29] R. Sheppard, D. Morgan, D. Mathes, and D Bray. Properties and characteristics of graphite. *Inc.: Decatur, TX, USA*, 2002.

[30] R. L Baker. Graphite sublimation chemistry nonequilibrium effects. *AIAA Journal*, 15(10):1391–1397, 1977. doi: 10.2514/3.60806.

[31] James Keenan and Graham Candler. Simulation of graphite sublimation and oxidation under re-entry conditions. In *6th Joint Thermophysics and Heat Transfer Conference*, page 2083, 1994. doi: https://doi.org/10.2514/6.1994-2083.

[32] Page Askins, Alexandre Martin, Benjamin Libben, Grant Palmer, and Joseph Williams. Semi-empirical 1d material response modeling using inverse methods. In *AIAA AVIATION 2022 Forum*, page 3730, 2022. doi: https://doi.org/10.2514/6.2022-3730.

[33] James B. Scoggins, Vincent Leroy, Georgios Bellas-Chatzigeorgis, Bruno Dias, and Thierry E. Magin. Mutation++: Multicomponent thermodynamic and transport properties for ionized gases in c++. *SoftwareX*, 12, 2020. doi: 10.1016/j.softx.2020.100575.